Regular Article

Microwave solvothermal carboxymethyl chitosan templated synthesis of TiO$_2$/ZrO$_2$ composites toward enhanced photocatalytic degradation of Rhodamine B

Jiangyang Tian [a], Qian Shao [a,*], Junkai Zhao [a], Duo Pan [a], Mengyao Dong [b,f], Chengxinzhuo Jia [c,*], Tao Ding [d,*], Tingting Wu [e], Zhanhu Guo [b,*]

[a] College of Chemical and Environmental Engineering, Shandong University of Science and Technology, Qingdao 266590, China
[b] Integrated Composites Laboratory (ICL), Department of Chemical & Biomolecular Engineering, University of Tennessee, Knoxville, TN 37996, USA
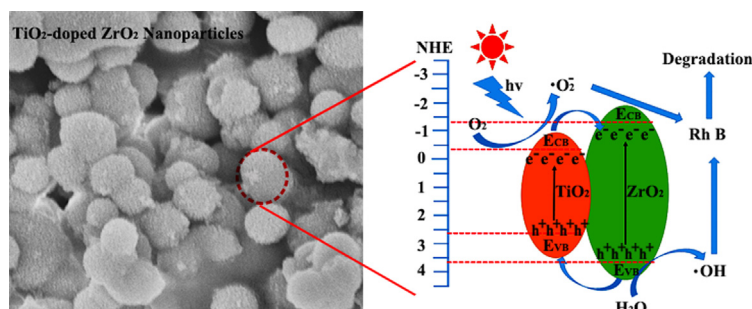[c] Eco-development Academy, Southwest Forestry University, Kunming Yunnan 650224, China
[d] College of Chemistry and Chemical Engineering, Henan University, Kaifeng 475004, China
[e] Department of Civil and Environmental Engineering, The University of Alabama, Huntsville, AL 35899, USA
[f] Key Laboratory of Materials Processing and Mold (Zhengzhou University), Ministry of Education; National Engineering Research Center for Advanced Polymer Processing Technology, Zhengzhou University, Zhengzhou 450002, China

GRAPHICAL ABSTRACT

ARTICLE INFO

ABSTRACT

A series of TiO$_2$/ZrO$_2$ composites with various molar ratios of ZrO$_2$:TiO$_2$ were synthesized by a facile and mild microwave hydrothermal method with carboxymethyl chitosan (CMCS) as templates. The as-obtained products were characterized with wide-angle powder X-ray diffraction (XRD), scanning electron microscopy (SEM), transmission electron microscopy (TEM), Fourier transform infrared spectroscopy (FTIR), UV–vis diffuse reflectance spectrophotometry (UV–vis-DRS), N$_2$ adsorption-desorption isotherms (BET), and X-ray photoelectron spectrometer (XPS). The TiO$_2$/ZrO$_2$ composites with heterogeneous structure consisted of particles which showed a better regularity and uniform with about 800 nm in diameter, and showed a larger specific surface area and smaller energy band gap than pure ZrO$_2$. Comparative experiments including varying the pH of the solution and the content of titania demonstrated that the 5% TiO$_2$/ZrO$_2$ composites ($n_{Ti}:n_{Zr}$ = 5:100) at pH = 10.3 possessed the best photocatalytic property. Moreover, the possible reasons for these phenomena were clarified. Cyclic experiments proved that the resulting TiO$_2$/ZrO$_2$ composites as photocatalyst could be reused efficiently. Meanwhile, a possible mechanism of photocatalysis was proposed.

© 2019 Elsevier Inc. All rights reserved.

---

* Corresponding authors.
  E-mail addresses: shaoqian01@126.com (Q. Shao), jiachenxinzhuo@126.com (C. Jia), dingtao@henu.edu.cn (T. Ding), zguo10@utk.edu (Z. Guo).

1. Introduction

With the rapid development in textile, leather, food and paper industries, dye contaminants of various water resources have caused great concerns because of their toxicity, carcinogenicity and mutagenicity [1]. Therefore, it is essential that dye stuffs are removed from wastewater before they are released [2–4]. An effective approach to eliminate effects of dye to the human race and nature is achieved by decomposing dye stuffs into organic molecules which are harmless to human health and nature with appropriate catalysts under the sunlight or UV-light [5–11].

Chitosan (CS) is one of linear copolymers of $\beta(1–4)$ linked 2-acetamido-2deoxy-β-D-glucopyranose and 2-amino-2-deoxy-β-D-glycopyranose [12]. The high content of amino and hydroxyl functional groups, acting as coordination sites to form complexes, endows chitosan the highest metal coordinating ability among the natural polymers, which makes it possible for chitosan to be used as an appropriate adsorbent and bio-template [13–15]. For instance, Jiang et al. synthesized mesoporous titania spheres using chitosan/ploy as template to decompose phenol in the water [16]. Meanwhile, chitin, the source of chitosan, can be widely obtained from crustaceans, insect, and certain fungi, of which output estimated to be several billion tons per year [17–19]. Thus, chitosan is considered as a non-toxic and easily available biocompatible biopolymer in nature [20]. However, the wide application of chitosan is restricted owing to poor chemical stability and low mechanical strength [21]. In order to solve these problems, an approach to modify chitosan is normally applied. For example, Fan et al. prepared a cross-linked magnetic chitosan with a higher performance of Zn^{2+} adsorption from aqueous solution [13]. In the reported studies, carboxymethyl chitosan (CMCS) was obtained by modifying CS with monochloro acetic acids, which contain more carboxyl, amino and hydroxyl functional groups. Compared to CS, CMCS not only can be applied in wider pH ranges of water since its higher stability, but also has a higher hydrophilicity [22]. The larger specific surface area, a multitude of functional groups and higher hydrophilicity of CMCS are expected to play an essential role in more efficiently coordinating with mental oxide and flocculate sol [23].

N-type semiconductor zirconia (ZrO_2) is commonly applied as catalysts, catalyst supports, dielectric material, chemical sensors and photocatalytic material due to its chemical inertness, excellent thermal stability, nontoxicity, re-usability and low cost [24–31]. On the other hand, pure ZrO_2 only absorbs 4% of solar light owing to poor specific surface area and higher energy band gap which are considered to be primary reasons to reduce effective electron transfer and charge separation, thus its large scale applications as photocatalysts have been greatly limited [32]. Many efforts to improve light response of semiconductor materials have been reported, such as metal ion and non-metal ion doping, semiconductor doping, dye sensitization, preparation of composites [33–36]. Among all the reported methods, metal ion and non-metal ion doping were considered as the most effective way to modify the properties of ZrO_2 [36]. For example, Renuka et al. synthesized multi-functional ZrO_2/CuO nanocomposites by a simple combustion, which showed outstanding photocatalytic properties under sunlight [37]. In addition, some methods to significantly enhance the specific surface area of materials have been developed by using microorganisms, biological and inorganic salt as templates to prepare various novel materials [38–40]. For instance, Zhao et al. reported ZrO_2 hollow microspheres by adopting pollen templates to remove dye from solution [41]. Fan et al. synthesized mesoporous TiO_2/ZrO_2 nanocomposites by sol-gel method with Pluronic and Macrogo 20000 as double templates to decompose the Rhodamine B in water [42]. Although the synthesis and photocatalytic performance of TiO_2/ZrO_2 composites have been reported, the

preparation of TiO_2/ZrO_2 composites with high photoelectrocatalytic performance by the microwave solvothermal method has note been reported yet.

In this work, TiO_2/ZrO_2-CMCS (CMCS was acted as template) composites were successfully prepared through a facile and mild microwave solvothermal method in an hour which was obviously shorter than that of conventional solvothermal method. The TiO_2/ZrO_2 composites obtained after calcination of TiO_2/ZrO_2-CMCS in the air presented better dispersity and uniform morphology. The photocatalytic performance of the samples was tested by measuring the degradation of the Rhodamine B (Rh B) aqueous solution under UV-light and the effects of the pH of the solution and the content of titania in composites on the photocatalystic efficiency were investigated. The mechanism for the enhanced photocatalystic efficiency was discussed in details.

2. Experimental

2.1. Preparation of CMCS

The CMCS was prepared as follows. In a typical procedure, 2.0 g NaOH solution (50 wt%) was added into 3.0 g chitosan and alkalified for 30 min. Afterward, 15.0 g monochloro acetic acid was added into the above mixture and stirred in a water bath at 90C for 30 min. The schematic diagram of the chemical reaction was depicted in Scheme 1. The pH of final mixture was adjusted to 7 by adding glacial acetic acid dropwise. The mixture was washed with distilled water and absolute ethanol several times. The CMCS was obtained and dried at 50 °C in the air.

2.2. Synthesis of TiO₂/ZrO₂ composites

Preparation of 2% TiO_2/ZrO_2 (nTi:nZr = 2:100) is as followed. 3.0 g CMCS was dispersed into 20 mL anhydrous ethanol and stirred for 3 h to obtain an anhydrous suspension of CMCS. 2.93 g N-butanol zirconium and 0.052 g butyl titanate were added dropwise into the above mixture under stirring constantly and then ultrasonically dispersed for 10 min. 0.5 mL distilled water was added dropwise into the above mixture and ultrasonically dispersed for 10 min. The mixture was transferred to microwave hydrothermal synthesis system and heated to 150 °C with a heating rate of 5 °C min⁻¹, then maintained at 150 °C for 30 min. The precipitate was collected by centrifugation, washed by deionized water and ethanol for three times, and dried at 50 °C in air. Then, the as-obtained sample was calcined at 600 °C in air for 3 h at a heating rate of 5 °C min⁻¹, and 2% TiO_2/ZrO_2 composites were obtained. Besides, other samples could be obtained with the same procedures by changing the mass of butyl titanate (0, 0.104, 0.13, 0.156, 0.208 g). Pure ZrO_2 (pure TiO_2) was prepared by the same procedures in the absence of butyl titanate (N-butanol zirconium) and templates. Meanwhile, the samples mentioned above were labelled and the details were listed in Table 1. For instance, T/Z-CMCS-5 represented the composites prepared by adding N-butanol zirconium and butyl titanate (nTi:nZr = 5:100) in the presence of CMCS as templates. T/Z-5 represented 5% TiO_2/ZrO_2 (nTi:nZr = 5:100) composites obtained by calcining T/Z-CMCS-5 at 600 °C.

2.3. Characterization

SEM images of the composites were taken with a field emission scanning electron microscopy (SEM, S-4800, Hitachi, Japan). Transmission electron microscope (TEM, FEI Talos F200S, Czech) was used to investigate the crystallize size and lattice plane D-spacing. X-ray power diffraction (XRD) patterns of the
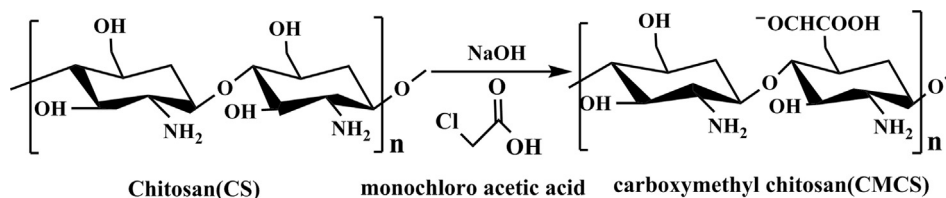
Scheme 1. Schematic diagram of chemical reaction of chitosan modified with carboxylic groups.

Table 1
Information of different samples.

CS as templates (g)	CMCS as templates (g)	[a]N-butanol zirconium (g)	[a]Butyl titanate (g)	[b]$\frac{n_{Ti}}{n_{Zr}}$ (%)	[c]Abbreviation before calcination	[c]Abbreviation after calcination
3.0	/	2.93	0.13	5	T/Z-CS-5	T/Z-S-5
0	0	0	2.60	100	Pure-T	P/T
0	0	2.93	0	0	Pure-Z	P/Z
/	3.0	2.93	0	0	T/Z-CMCS-0	T/Z-0
/	3.0	2.93	0.052	2	T/Z-CMCS-2	T/Z-2
/	3.0	2.93	0.104	4	T/Z-CMCS-4	T/Z-4
/	3.0	2.93	0.130	5	T/Z-CMCS-5	T/Z-5
/	3.0	2.93	0.156	6	T/Z-CMCS-6	T/Z-6
/	3.0	2.93	0.208	8	T/Z-CMCS-8	T/Z-8
/	3.0	0	2.60	100	T/Z-CMCS-100	T/Z-100

[a] The mass of chemical reagents added to prepared different samples.
[b] The molar ratio of Zr and Ti element in the added ester.
[c] Abbreviation of different composites.

as-prepared samples were acquired by a Rigaku D/Max 2400X-ray diffractometer (XRD, ultima IV, Rigaku, Japan) with graphite monochromatized Cu Kα radiation (30 kV, 100 mA). FTIR spectra were recorded from KBr pellets on a NACOLET 380 FT-IR spectrometer (Nicolet Thermo, USA). The diffuse reflectance UV–visible spectrum of sample was recorded on a UV-2550 UV–visible spectrophotometer (UV–Vis DRS Hitachi, UH4150, Japan). Thermal stability was studied by a thermogravimetric analyser (TGA, NETZSCH STA 449F3, Japan) at heating rate of 10 °C min^{-1} in air atmosphere from 298 to 1073 K. The BET determinations were carried by using BELSORP-Mini II apparatus (Microtrac Bel Co. Ltd, Japan) and the pore size distribution was obtained based on Barrett-joyner-Halenda (BJH). Elemental composition information of samples were done by an ESCALAB 250Xi X-ray photoelecton spectrometer (XPS, Thermo Scientific, USA) with a monochromatic Al K-Alpha radiation (150 W, 15 KV, and 1486 eV).

2.4. Photocatalytic experiments

50.0 mg as-obtained samples were added into 100.0 mL Rh B aqueous solution (10 mg L^{-1}, pH = 8.0). The mixture reaching adsorption equilibrium after treating in the dark for 60 min was transferred to the photochemical reactor under irradiation of UV-light (CEL-LPH120). The pH of Rh B aqueous solution was adjusted by 0.1 mol L^{-1} HCl aqueous solution and 0.1 mol L^{-1} NaOH aqueous solution. At regular intervals, the absorbance of a certain amount of solution was measured by UH-4150 UV–visible absorption spectrophotometer at maximum absorption wavelength of Rh B (554 nm).

3. Results and discussion

3.1. Characterizations of the photocatalysts

The XRD patterns of the as-obtained samples are shown in Fig. 1. In Fig. 1a, all the diffraction patterns of TiO$_2$/ZrO$_2$ composites with different contents of TiO$_2$ show peaks at 30.50, 35.65, 50.72,
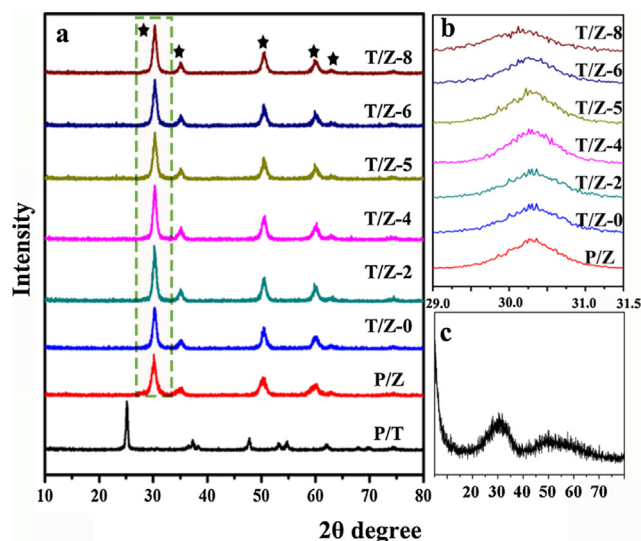

Fig. 1. XRD patterns of (a) composites after calcination, (b) the (1 0 1) plane of composites intercepted from (a), and (c) the T/Z-CMCS-5.

60.11 and 63.88°, which can be assigned to the (1 1 1), (2 0 0), (2 2 0), (3 1 1) and (2 2 2) crystal planes of the tetragonal ZrO$_2$ (JCDPS # 50-1089), respectively. Comparing the XRD patterns of T/Z composites with that of P/Z, there are no additional peaks occurring, demonstrating that T/Z composites are of high purity and good crystallinity. The reason of no significant peaks assigned to the titanium oxide may be attributed to the low content of TiO$_2$ in the composites [43]. Fig. 1b shows the (1 1 1) diffraction peaks of TiO$_2$/ZrO$_2$ composites. As the content of TiO$_2$ in TiO$_2$/ZrO$_2$ composites increases, the (1 1 1) diffraction peaks shift to a lower angle, which can be attributed to the recombination of TiO$_2$ into ZrO$_2$ [44]. Further, the average crystallite size can be calculated by Debye-Scherrer Equation [37] and the results are depicted in Table 2. It can be seen that the TiO$_2$/ZrO$_2$ composites with different

Table 2
The average crystallite size of samples.

Samples	T/Z-0	T/Z-2	T/Z-4	T/Z-5	T/Z-6	T/Z-8
Average crystallite size (nm)	10.5	10.7	11.3	12.7	10.5	10.2

content of TiO_2 show various average crystallite size, which may be attributed to different nuclei and coordination geometry of ZrO_2 and TiO_2 [45]. Since the XRD patterns of T/Z-CMCS with different contents of TiO_2 are analogous, the XRD pattern of T/Z-CMCS-5 (Fig. 1c) is shown as a representative. The broad diffraction bands of T/Z-CMCS-5 composite reveal that the sample before calcination is amorphous.

XPS measurement is carried out to investigate the surface composition of T/Z-5 and the results are listed in Fig. 2. Three peaks appearing on Fig. 2a correspond to titanium (2p), oxygen (1s), and zirconium (3d) states, respectively. The twin peaks in Fig. 2b of Zr 3d with the binding energies at 182.1 and 184.3 eV correspond to the Zr $3d_{3/2}$ and Zr $3d_{5/2}$ chemical states, respectively, which indicate zirconium in the +4 oxidation states and the presence of Zr—O [46]. In addition, there are two peaks at 181.7 and 184.8 eV, suggesting the existence of Zr—Ti chemical bonds in the composites [47]. The Ti 2p peaks in Fig. 2c located at 458.6 eV and 464.4 eV correspond to Ti $2p_{1/2}$ and Ti $2p_{3/2}$ chemical states, respectively. The peaks of Ti verify the existence of Ti^{4+} oxidation state in the composite and the presence of Ti—O. Meanwhile, there is an inconspicuous peak at 465.0 eV, which can be attributed to the Zr—Ti chemical bonds [48]. The existence of Zr—O, Ti—O and Zr—Ti chemical bonds indicates the phase contact between TiO_2 and ZrO_2. It can be observed in Fig. 2d that the O 1s binding energy appears at 530.0 eV, which is a proof of presence of crystal lattice oxygen (O^{2-}) [49]. The mole ratio of TiO_2 to ZrO_2 in T/Z-5 is estimated to be about 4.7% based on the peak area on the XPS spectra (Fig. 2b and d), which is close to the theoretical value (5%).

The morphologies of T/Z-CMCS-5 and T/Z-5 composites were imaged by SEM. It can be clearly seen from Fig. 3b that the agglomerated particles of T/Z-CMCS-5 show an average diameter of 800–900 nm and the morphology of sample is similar to the coral rock. Fig. 3d–f shows the images of T/Z-5 at different magnifications. Compared with T/Z-CMCS-5 in Fig. 3a, the morphology of T/Z-5 in Fig. 3d and e has no significant change. Meanwhile, the roughness degree of the sample surface after calcination (Fig. 3f and g) increases significantly, which can be attributed to release of gas generating by organic templates in the process of calcination. Due to the loss of the CMCS templates, the volume of particle (about 800 nm) decreases slightly. The disappearance of the CMCS leads to the obviously improved particle dispersity.

Fig. 4 shows the TEM photograph of T/Z-5. The morphologies of T/Z-5 can be clearly observed from Fig. 4a–c, which is in agreement with the SEM results. As shown in Fig. 4d and e, two sets of lattice fringe spacings of 0.337 nm and 0.202 nm are corresponding to the d-spacing of (1 1 1) plane of ZrO_2 and (1 0 1) plane of TiO_2. Owing to the introduction of TiO_2 into ZrO_2 during the stages of synthesis, the lattice mismatch appears at the interface of ZrO_2 and TiO_2 and further lead to a disoriented atomic arrangement [50]. According to the results of XRD, XPS and SAED analyses, it can be concluded that the composites are composed of TiO_2 and ZrO_2 with heterogeneous structure. Element mapping of T/Z-5 (Fig. 4f– h) reveals that Ti, O and Zr elements are uniformly distributed in entire composites. With respect to all these structural analysis results, it is proved that TiO_2 effectively built into the ZrO_2 host matrix.

The FT-IR spectra of the raw CS, CMCS and T/Z-CMCS in the range 500–4000 cm^{-1} are shown in Fig. 5. The predominant peaks
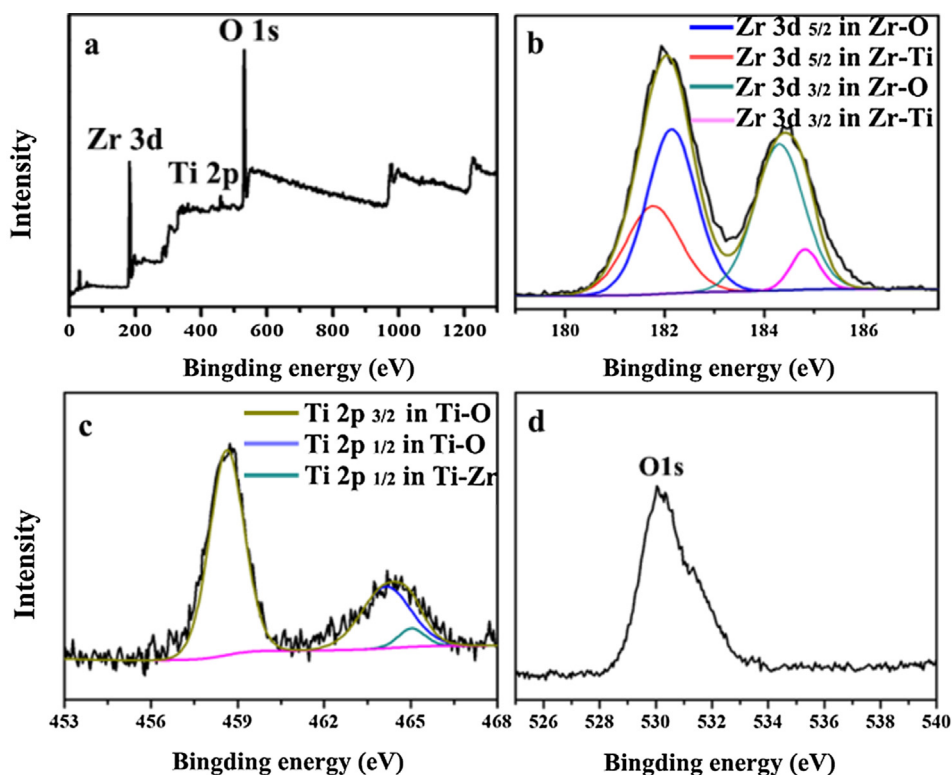

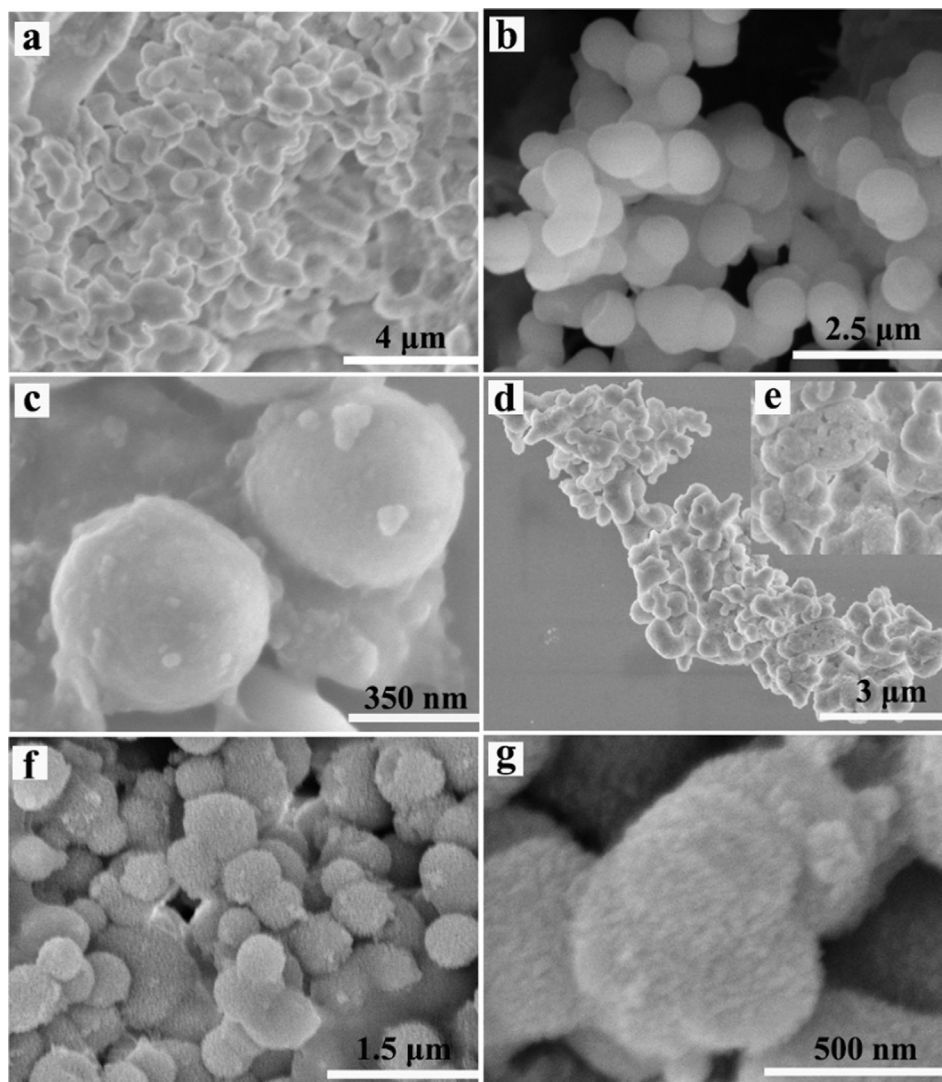**Fig. 2.** XPS full survey spectrum of T/Z-5 (a), the XPS spectra of Zr 3d (b) and Ti 2p (c), O 1s (d) in T/Z-5.

Fig. 3. SEM images of T/Z-CMCS-5 (a-c), T/Z-5 (d, f, g) and local enlarged image of (d) (inset (e)).

at 3450, 1600 and 1200 cm^{-1} are assigned to the O—H bending vibrations, N—H bending vibrations and C—O—C bending vibrations, respectively [51]. The occurrence of peaks (in b) at 1490 cm^{-1} owing to the —COOH bending vibrations demonstrates that CS is modified by monochloro acetic acid successfully. The peak at 780 cm^{-1} corresponds to the Zr—O—Zr vibration, while the inconspicuous peak at 1100 cm^{-1} confirms the presence of Ti—O stretching vibration [34]. The broad peak ranging from 3750 to 3250 cm^{-1} correspond to the surface hydroxyl groups which are attributed to CMCS templates and the physically adsorbed water molecules in the CMCS templates.

TG curve of T/Z-CMCS-5 is shown in Fig. 6. There is an initial weight loss about 10 wt% below 200 °C, which is mainly attributed to the release of water adsorbed by CMCS from air or existing in the template molecules. The next weight loss of approximate 30 wt% below 600 °C corresponds to the decomposition of CMCS templates. There is no significant loss in weight when the temperature is over 600 °C. The TGA result demonstrates the weight ratio of templates in samples is about 30% and the appropriate calcination temperature is 600 °C.

Pore structure and specific surface area changes due to the presence of TiO_2 were investigated by comparing N_2 adsorption/desorption isotherms. The accumulated pore size distributions of P/Z and T/Z-5 are illustrated in Fig. 7. It is obvious in Fig. 7a that the physisorption isotherm of the P/Z is of type IV while T/Z-5 is of type V, indicating a typical mesoporous structure with a relatively wide pore size distribution [16]. Based on the isotherm pattern, T/Z-5 shows a larger specific surface area of 72.8 $m^2\,g^{-1}$ which is 4 times larger than that of P/Z sample (22.5 $m^2\,g^{-1}$). Meanwhile, the average pore size value of T/Z-5 (Fig. 7b) is observed approximate 11 nm while the value of P/Z is about 5 nm. The samples (T/Z-5) prepared in the presence of templates shows a larger specific surface area, suggesting more active sites are provided in the process of photocatalysis. Hence, the enhancements of specific surface area and average pore size of the samples are considered as one of the favorable conditions to enhance photocatalytic activity for Rh B dye degradation.

The UV–vis absorption spectra of the T/Z, T/Z-100 and T/Z-0 are shown in Fig. 8a and b. The results of $(Ah\nu)^2$ based on indirect allowed transition for the photon energy of the samples are shown in Fig. 8c and d. The band gap of the all samples can be obtained based on Tauc' s Equation [37] and the results are shown in Table 3. Fig. 8a and b show that the absorption edge of all samples is at ~360 nm. Compared with T/Z-0 particles, the absorption intensities of all T/Z samples are obviously larger in the UV-light region. The results in Table 3 show the band gap energy of T/Z-100 and
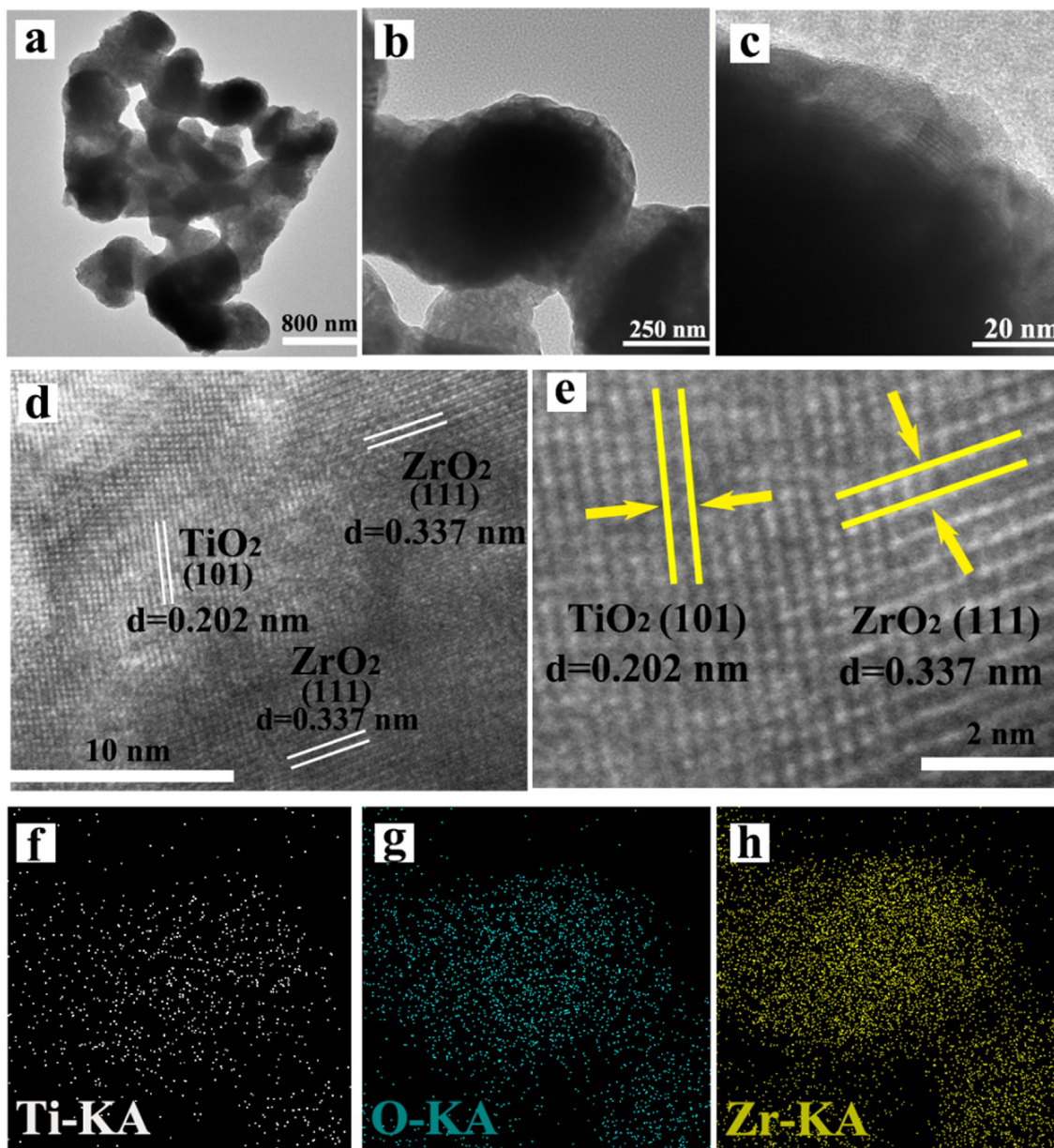
Fig. 4. TEM images (a-c), HRTEM images (d, e) and Element mapping images (f–h) of T/Z-5.

T/Z-0 is 3.26 and 5.21 eV, respectively. Compared with T/Z-0 particles, the band gap energies of all the TiO$_2$/ZrO$_2$ samples decrease significantly and are between 3.96 and 3.78 eV. The decrease in the band gap for all TiO$_2$/ZrO$_2$ samples compared to T/Z-0 can be attributed to lower band gap of TiO$_2$ [52]. The result facilitates the separation of electrons and holes pair during light irradiation, which eventually leads to the faster photocatalytic dye degradation.

3.2. Photocatalytic activity

3.2.1. Effect of the TiO$_2$ content

Fig. 9a shows the corresponding photocatalytic efficiency by using TiO$_2$/ZrO$_2$ composites as catalyst towards Rh B dye degradation. The maximum absorption wavelength of Rh B is observed at 554 nm in Fig. 9b. The dye degradation efficiency can be calculated according to Eq. (1):

$$\text{Degradation efficiency} = \frac{A_0 - A_t}{A_0} \quad (1)$$

where A_0, A_t is the absorbance of Rh B solution at maximum absorption wavelength after treating in dark for 60 min and after reacting for t min, respectively. The order of degradation efficiency of all samples is as follows: T/Z-5 (degradation efficiency: 90.5%) > T/Z-4 (degradation efficiency: 85.5%) > T/Z-6 (degradation efficiency: 82.6%) > T/Z-8 (degradation efficiency: 75.7%) > T/Z-2 (degradation efficiency: 73.9%) > T/Z-0 (degradation efficiency: 60.6%). Compared with T/Z-0 particles, the dye degradation efficiency of all T/Z samples increases obviously, which illustrates that the compositing of TiO$_2$ into ZrO$_2$ can reduce electron-hole pair recombination and shows a better catalytic efficiency. As the content of TiO$_2$ increases, the degradation efficiency increases gradually until the mole ratio of TiO$_2$ to ZrO$_2$ reaches 5%, and then the degradation efficiency decreases. The recombination of TiO$_2$ results in the lattice expansion of ZrO$_2$, but as the mole ratio of TiO$_2$ to ZrO$_2$ exceeds 5%, the
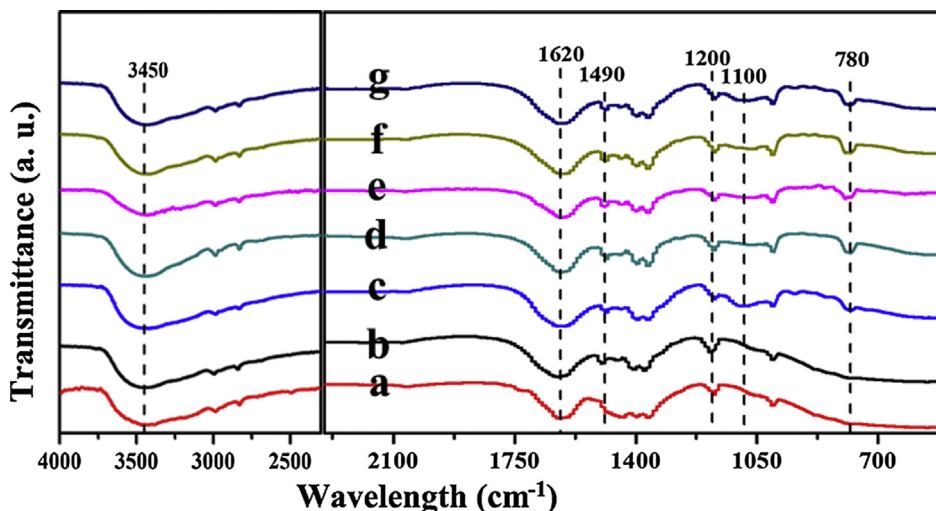
Fig. 5. FT-IR spectra of the raw CS (a), CMCS (b), T/Z-CMCS-8 (c), T/Z-CMCS-6 (d), T/Z-CMCS-5 (e), T/Z-CMCS-4 (f) and T/Z-CMCS-2 (g).
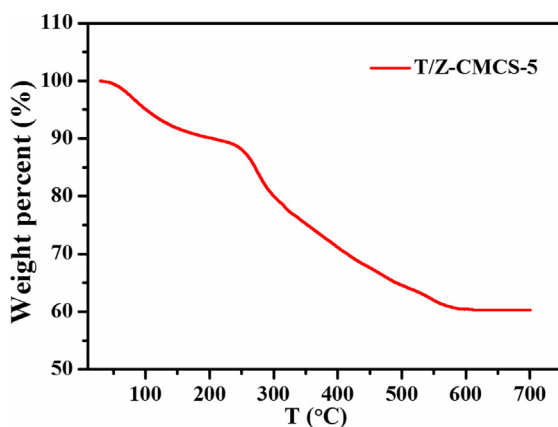

Fig. 6. TG curve of T/Z-CMCS-5 sample.

structural defect of T/Z composites occurs owning to the lattice expansion. Eventually, the degradation efficiency of samples reduces [43]. Thus 5% of TiO$_2$ is regarded as the optimum content and T/Z-5 is used as suitable photocatalyst for further photocatalytic experiments.
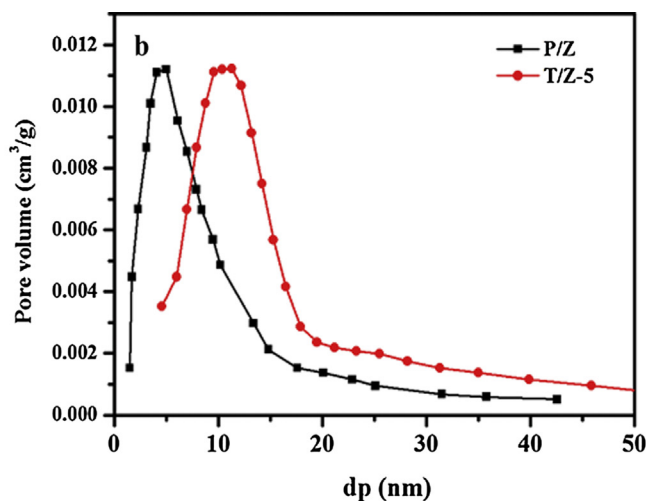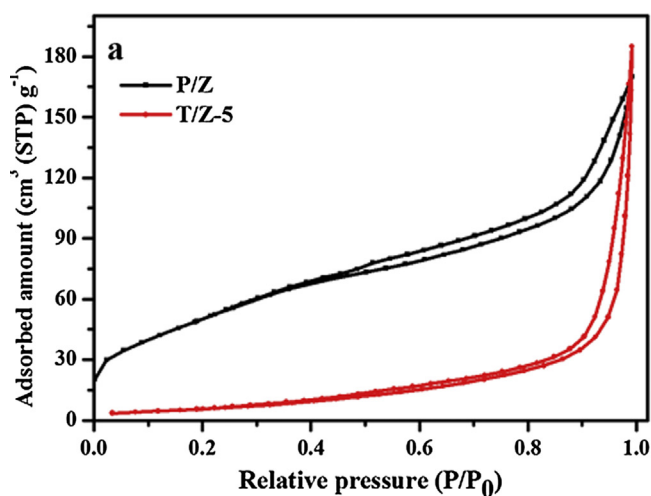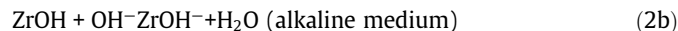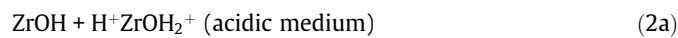
3.2.2. Effect of the pH of Rh B solution

In the process of photocatalytic, the pH of solution is not a negligible factor influencing the performance of catalyst. Therefore, the degradation efficiency of Rh B with various pH values in the presence of T/Z-5 as photocatalyst under UV-light is measured and the results are shown in Fig. 10. The zirconium oxides maybe exist in varying degrees of protonation (2a) and deprotonation (2b) [53]:

$$ZrOH + H^+ZrOH_2^+ \text{ (acidic medium)} \qquad (2a)$$

$$ZrOH + OH^-ZrOH^- + H_2O \text{ (alkaline medium)} \qquad (2b)$$

As the pH increases from 5.4 to 10.3, the photocatalytic efficiency of Rh B degradation promotes. The enhancement of photocatalytic degradation is attributed to the ionic state of the Rh B molecules in the aqueous solution. The attractive electrostatic forces existing between the negatively charged ZrO$_2$ surface and the positively charged dye molecules groups strengthen gradually with increasing the pH value, and can eventually facilitate more efficient decomposition of dyes. As the pH value increases to higher than 10.3, the photoexcitation happening on the catalyst surface will be masked because of non-adsorption of the undissociated
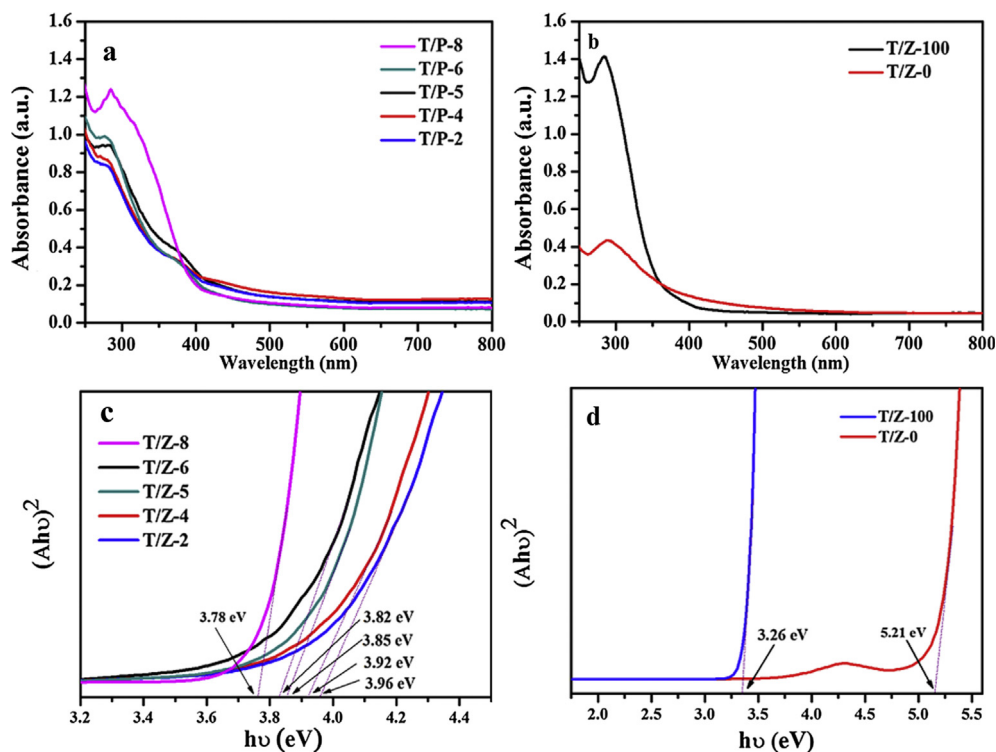

Fig. 7. N$_2$ sorption isotherms (a) and accumulated pore size distribution (b).

Fig. 8. UV–visible spectra of the T/Z (a), T/Z-100, T/Z-0 (b) and the plotting of $(Ah\upsilon)^2$ *vs.* $h\upsilon$ based on the indirect allowed transition (c) and (d).

Table 3
The band gap of samples.

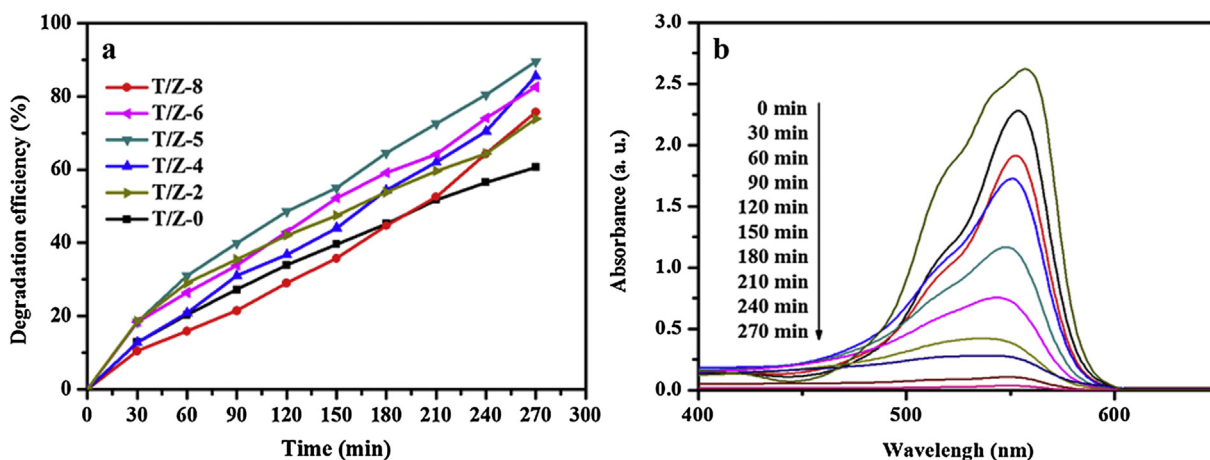| Samples	T/Z-0	T/Z-2	T/Z-4	T/Z-5	T/Z-6	T/Z-8	T/Z-100
Band gap (eV)	5.21	3.96	3.92	3.85	3.82	3.78	3.26

Fig. 9. Degradation efficiency of Rh B using TiO_2/ZrO_2 composites (a), the absorption spectra of Rh B with T/Z-5 as photocatalyst in different reaction time (b).

dye molecules and its dispersion in the bulk solution, which leads to less production of reactive free radicals (OH·) followed by low photocatalytic efficiency [43]. Otherwise, the electrostatic forces between positively charged ZrO_2 in acidic solution and the positively charged dye molecules groups turn into exclusion rather than attraction, so photocatalytic efficiency reduces.

3.2.3. Effect of different catalysts on Rh B

The degradation efficiencies of Rh B for different samples under the UV-light were evaluated. The results are shown in Fig. 11. Com-

pared with the photocatalytic properties of P/Z particle, the enhanced photocatalytic property of T/Z-0 is attributed to the enlargement of specific surface area to provide more active sites that can play a significant role for absorption of UV-light. Meanwhile, the result that T/Z-5 shows a better degradation efficiency than T/Z-S-5 illustrates that CS after being modified (CMCS) shows a better performance as templates. Furthermore, it can be seen that the photocatalytic activity of T/Z-5 is approximately 30% higher than that of T/Z-0 samples, illustrating that the compositing of TiO_2 into ZrO_2 causes a slow electron-hole pair recombination rate
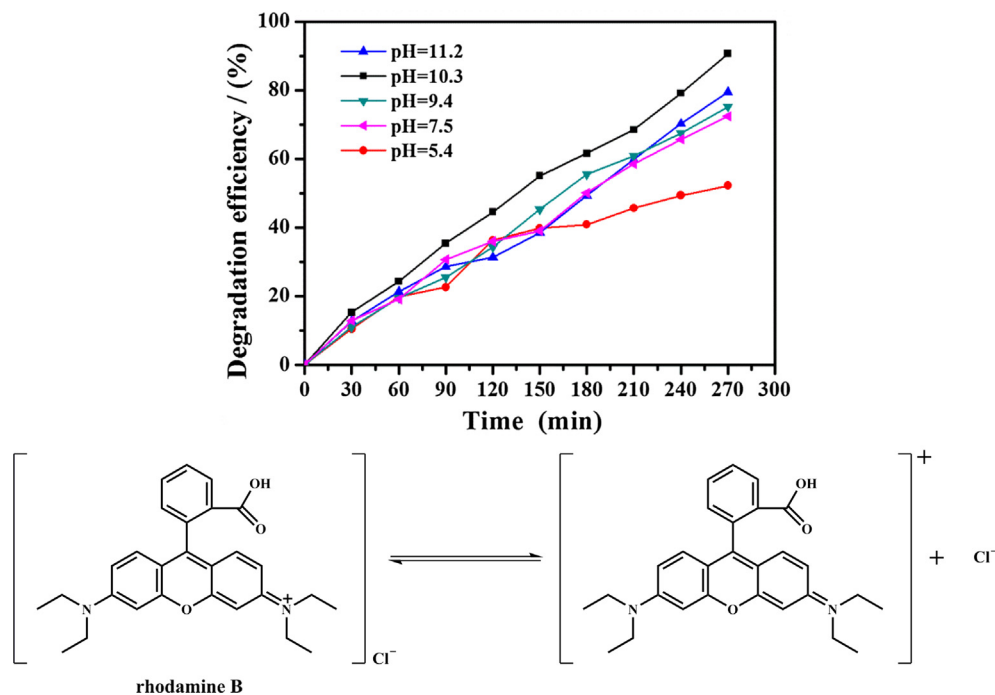
Fig. 10. Degradation efficiency of Rh B solution with various pH values and schematic diagram of Rh B hydrolysis.

with fast electron transfer ability. Therefore, T/Z-5 prepared by using CMCS as templates performs the best photocatalytic degradation efficiency in comparison with other samples.

3.2.4. Reusability experiment

The stability of the photocatalyst is considered to play a pivotal role in evaluating the performance of catalyst, the cyclic experiments are conducted for six runs and the result is depicted in Fig. 12a. After the first measurement, the catalyst is centrifuged, then washed three times with deionized water and ethanol, and dried for the next cyclic experiment. The catalyst is added into the freshly prepared dye solution and the previous experiment steps are repeated. The data of photocatalytic experiments in Fig. 12a and SEM image of catalyst after six cycles in Fig. 12b reveal that there is no appreciable loss in the activity and obvious change in the morphology of catalyst, which demonstrates that the photocatalyst is photostable and can be reused efficiently. Meanwhile, the photocatalytic activities of other reported ZrO_2 particles are compared and listed in Table 4. In the case of achieving the same
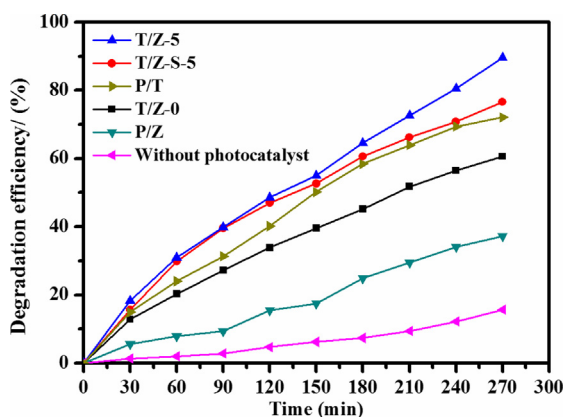

Fig. 11. Degradation efficiency of Rh B with various catalysts.

degradation efficiencies, some aspects of TiO_2/ZrO_2 composites including the time to prepare samples, applicable pH range and recyclable times show the obvious superiority.

3.3. Photocatalytic mechanism

The conduction band (CB) and valence band (VB) of samples can be calculated according to Eqs. (3a) and (3b) [37]:

$$E_{CB} = X - E^c - 0.5E_g \tag{3a}$$

$$E_{VB} = X - E^c + 0.5Eg \tag{3b}$$

where E_{CB}, E_{VB} is the CB and VB edge potential, respectively; X is the electronegativity of the semiconductor, which is the geometric mean of the electronegativity of the constituent atoms (The X value of ZrO_2 and TiO_2 are 5.91 and 5.81 [58]; E^c is the energy of free electrons on the hydrogen scale (4.5 eV); and E_g is the band gap energy of the semiconductor (The E_g values of ZrO_2 and TiO_2 are calculated to be 5.21 and 3.26 eV as shown in Fig. 7, respectively.). According to the above relation, the E_{CB} values of ZrO_2 and TiO_2 are calculated to be −1.195 and −0.32 eV, while the E_{VB} are 4.015 and 2.94 eV, respectively.

Based on aforementioned experimental results, the mechanism of the photocatalytic degradation is proposed. As shown in Fig. 13, the photocatalytic mechanism mainly can be analyzed by three stages and the detailed progress is described as follows: (I) The light absorption of the material and the production of charge carriers (electrons and holes) (Eqs. (4a)). Under the sunlight radiation, the transition of electrons from the VB of ZrO_2 and TiO_2 to CB occurred and the same number of holes left in the corresponding valence band position. (II) The transfer of electrons and holes. Compared with E_{CB} value of TiO_2 (−0.32 eV), the E_{CB} value of ZrO_2 (−1.195 eV) is more negative, which results in the electrons move from the CB of ZrO_2 to the CB of TiO_2. Meanwhile, the holes will migrate from VB of TiO_2 to VB of ZrO_2. (III) The reaction between charge carries and reactants (Eqs. (4b)–(4e)). The superoxide radical ($·O_2^-$) is generated from the interactions between produced
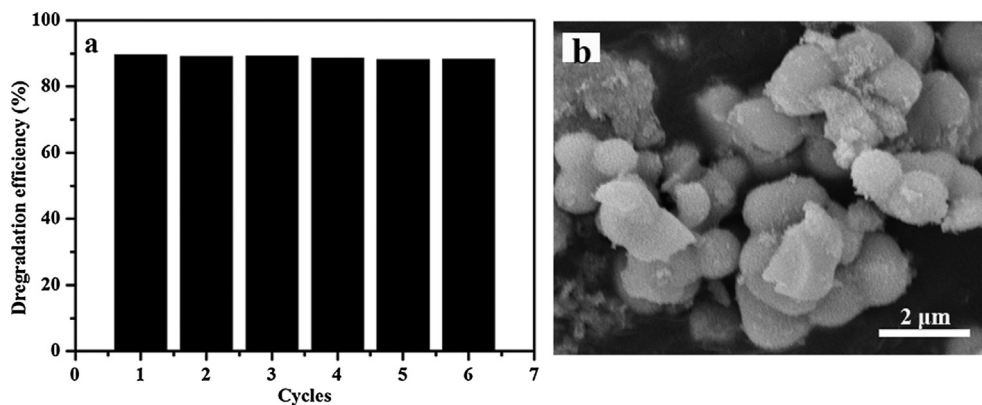
Fig. 12. The cycles of photocatalytic experiment of T/Z-5 (a) and SEM image (b) of catalyst after using six cycles.

Table 4
Comparison of photocatalytic activity of several ZrO_2 particles.

[a]Samples	[b]Methods	[c]Mass (mg)	[d] Catalytic efficiency	[e]pH	[f]Cycles	Reference
Dye	Time	$V \times c$ (L × mg/L)				
N-ZrO_2	Thermal Decomposition	100	84.5%	5–9	6	[54]
Amaranth	24 h	0.1 × 10	after 4 h			
ZrO_2	Hydrothermal	50	90.0%	/	/	[55]
2.4.6-Trichlorophenol	24 h	0.1 × 10	after 4 h			
Pd-ZrO_2-MWCNTs	Co-precipitation	100	95.0%	/	/	[56]
Acid Blue 40	12 h	0.1 × 20	after 4 h			
Fe_3O_4@ZrO_2	Sol-gel	50	89.0%	/	5	[57]
Methyl Orange	14 h	0.05 × 10	after 4 h			
TiO_2/ZrO_2	Microwave solvothermal	50	90.5%	7–11	6	This work
Rh B	1.0 h	0.1 × 10	after 4.5 h			

[a] Sample that shows the best photocatalytic property is selected as representative.
[b] The method to prepared the catalyst and the reaction time.
[c] The mass of samples, the volume and concentration of dye solution is added in photocatalytic experiment.
[d] The degradation efficiency of catalysts and the time required.
[e] The pH of dye solution in which the degradation efficiency of photocatalyst still reach over 75%.
[f] The cycles in which the degradation efficiency of sample has no change obviously.

electrons and atmospheric oxygen, while hydroxyl radical (·OH) is produced by the holes present in the valence band and water molecules. The formation of radicals can not only avoid electron-hole recombination efficiently but also breakdown the bonds existing in the dye molecules and degrade it completely [59]. The mechanism can be described approximately based on the following reactions (4a)–(4e):

$$ZrO_2/TiO_2 + h\upsilon \rightarrow ZrO_2\ (h^+) + TiO_2\ (e^-) \tag{4a}$$

$$TiO_2\ (e^-) + O_2 \rightarrow ·O_2^- + TiO_2 \tag{4b}$$

$$h^+ + OH^- \rightarrow 2·OH \tag{4c}$$

$$·O_2^- + Dye \rightarrow Degradation \tag{4d}$$

$$·OH + Dye \rightarrow Degradation \tag{4e}$$

4. Conclusions

A simple, efficient and environmentally friendly microwave solvothermal method was utilized to synthesize TiO_2/ZrO_2 composites in an hour. Based on the characterization of samples, the 5% TiO_2/ZrO_2 composites with a uniform diameter 800 nm exhibited a significantly enhanced specific surface area and reduced band gap, which led to a better photocatalytic degradation. 90.5% of Rh B was degraded under UV light irradiation in presence of 5% TiO_2/ZrO_2 composites as photocatalyst. Further, it was also proved that TiO_2/ ZrO_2 composites showed a better photocatalytic performance in alkaline solution (pH = 10.3) than other samples. Finally, the results about cycles experiment indicated there is no appreciable loss in degradation efficiency of samples over at least six cycles. Therefore, TiO_2/ZrO_2 composites prepared by microwave solvothermal method with less preparation time exhibit excellent photocatalytic degradation performance for dye, and show potential industrial applications in the environmental remediation. Meanwhile, these unique composites with unique dielectric
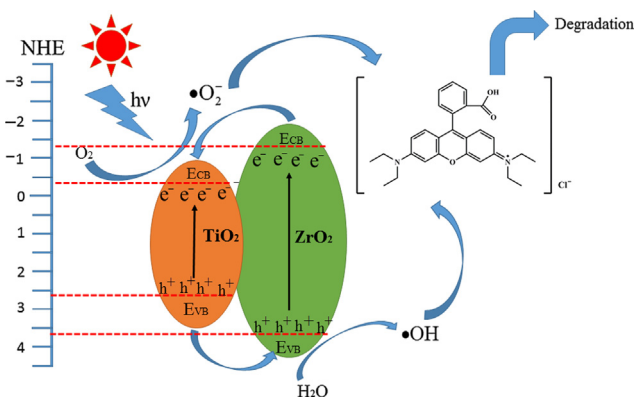

Fig. 13. Mechanism for the photocatalytic degradation of Rh B.

properties can be used for other applications if combined with polymer, metal, ceramic or carbon matrix [60–78] including sensors, electromagnetic interference (EMI) shielding, adsorbents for other pollutants or precious metal recovery from ocean, etc [79–89].

Appendix A. Supplementary material

Supplementary data to this article can be found online at https://doi.org/10.1016/j.jcis.2019.01.069.

References

[1] H.L. Jiang, P.H. Chen, S.L. Luo, X.B. Luo, X.M. Tu, Q. Cao, Synthesis of novel biocompatible composite Fe3O4/ZrO2/chitosan and its application for dye removal, J. Inorg. Organomet. 23 (2013) 393–400.
[2] T.H. Wu, Q. Shao, S.S. Ge, L.W. Bao, Q.Y. Liu, The facile preparation of novel magnetic zirconia composites with the aid of carboxymethyl chitosan and their efficient removal of dye, RSC Adv. 6 (2016) 58020–58027.
[3] K.D. Gong, Q. Hu, L. Yao, M. Li, D.Z. Sun, Q. Shao, Z.H. Guo, Ultrasonic pretreated sludge derived stable magnetic active carbon for Cr(VI) removal from wastewater, ACS Sustain. Chem. Eng. 6 (2018) 7283–7291.
[4] Z.Z. Li, B. Wang, X.M. Qin, Y.K. Wang, C.T. Liu, Q. Shao, N. Wang, Z.H. Guo, Superhydrophobic/superoleophilic polycarbonate/carbon nanotubes porous monolith for selective oil adsorption from water, ACS Sustain. Chem. Eng. 6 (2018) 13747–13755.
[5] B.M. Pirzada, N.A. Mir, N. Qutub, O. Mehraj, S. Suhail, Synthesis, characterization and optimization of photocatalytic activity of TiO2/ZrO2 nanocomposite heterostructures, Mater. Sci. Eng: B 193 (2015) 137–145.
[6] Z.Y. Zhao, H. An, J. Lin, M.C. Feng, V. Murugadoss, T. Ding, H. Liu, Q. Shao, X.M. Mai, N. Wang, H.B. Gu, S. Angaiah, Z.H. Guo, Progress on the photocatalytic reduction removal of chromium contamination, Chem. Rec. (2018), https://doi.org/10.1002/tcr.201800153 (in press).
[7] T.M. Su, Q. Shao, Z.Z. Qin, Z.H. Guo, Z.L. Wu, Role of interfaces in two-dimensional photocatalyst for water splitting, ACS Catal. 8 (2018) 2253–2276.
[8] L. Zhang, W. Yu, C. Han, J. Guo, Q.H. Zhang, H.Y. Xie, Q. Shao, Z.G. Sun, Z.H. Guo, Large scaled synthesis of heterostructured electrospun TiO2/SnO2 nanofibers with an enhanced photocatalytic activity, J. Electrochem. Soc. 164 (2017) 651–656.
[9] L. Zhang, M.K. Qin, W. Yu, Q.H. Zhang, H.Y. Xie, Z.G. Sun, Q. Shao, X.K. Guo, L.H. Hao, Heterostructured TiO2/WO3 nanocomposites for photocatalytic degradation of toluene under visible light, J. Electrochem. Soc. 164 (2017) H1086–H1090.
[10] B. Song, T.T. Wang, H.G. Sun, Q. Shao, J.K. Zhao, L.H. Hao, Z.H. Guo, Two-step hydrothermally synthesized carbon nanodots/WO3 photocatalysts with enhanced photocatalytic performance, Dalton. Trans. 46 (2017) 15769–15777.
[11] Y.Y. Sheng, J. Yang, F. Wang, L.C. Liu, H. Liu, C. Yan, Z.H. Guo, Sol-gel synthesized hexagonal boron nitride/titania nanocomposites with enhanced photocatalytic activity, Appl. Surface Sci. 465 (2019) 154–163.
[12] Y.C. Huang, Y. Wu, W.C. Huang, F. Yang, Degradation of chitosan by hydrodynamic cavitation, Polym. Degrad. Stabil 98 (2013) 37–43.
[13] L.L. Fan, C.N. Luo, F.G. Lu, H.M. Qiu, Preparation of magnetic modified chitosan and adsorption of Zn²⁺ from aqueous solutions, Colloid. Surface: B 88 (2011) 574–581.
[14] W.H. Wang, X.P. Hao, S.G. Chen, Z.Q. Yang, C.Y. Wang, R. Yan, X. Zhang, H. Liu, Q. Shao, Z.H. Guo, pH-responsive capsaicin@chitosan nanocapsules for antibiofouling in marine applications, Polymer 158 (2018) 223–230.
[15] H.B. Gu, X.J. Xu, H.Y. Zhang, C.B. Liang, H. Lou, C. Ma, Y.J. Li, Z.H. Guo, J.W. Gu, Chitosan-coated-magnetite with covalently grafted polystyrene based carbon nanocomposites for hexavalent chromium adsorption, Eng. Sci. 1 (2018) 46–54, https://doi.org/10.30919/espub.es.180308.
[16] R. Jiang, H.Y. Zhu, H.H. Chen, J. Yao, Y.Q. Fu, Z.Y. Zhang, Y.M. Xu, Effect of calcination temperature on physical parameters and photocatalytic activity of mesoporous titania spheres using chitosan/ploy (vinyl alcohol) hydrogel beads as a template, Appl. Surf. Sci. 319 (2014) 189–196.
[17] M.N.V.R. Kumar, A review of chitin and chitosan applications, Reactive Funct. Polym. 46 (2000) 1–27.
[18] A. Tolaimate, J. Desbrieres, M. Rhazi, A. Alagui, M. Vicedon, On the influence of deacetylation process on the physicochemical characteristics of chitosan from squid chitin, Polymers 41 (2000) 2463–2469.
[19] J.P. Latgé, The cell wall: a carbohydrate armour for the fungal cell, Mol. Microbiol 66 (2007) 279–290.
[20] K. Kurita, Chemical Modifications of Chitin and Chitosan [M]//Chitin in Nature and Technology, Springer, Boston, MA, 1986, pp. 287–293.
[21] E. Guibal, Interactions of metal ions with chitosan-based sorbents: a review, Sep. Purif. Technol. 38 (2004) 43–74.
[22] Z. Yang, B.O. Yuan, X. Huang, J.Y. Zhou, J. Cai, H. Yang, A.M. Li, Evaluation of the flocculation performance of carboxymethyl chitosan-graft-polyacrylamide, a novel amphoteric chemically bonded composite flocculant, Water. Res. 46 (2012) 107–114.
[23] G. Crini, Kinetic and equilibrium studies on the removal of cationic dyes from aqueous solution by adsorption onto a cyclodextrin polymer, Dyes. Pigments 77 (2008) 415–426.
[24] M. Labaki, H. Laversin, E.A. Zhilinskaya, A. Aboukais, D. Courcot, Electron Paramagnetic Resonance investigation of the nature of active species involved in carbon black oxidation on ZrO2 and Cu/ZrO2 catalysts, Catal. Commun. 17 (2012) 64–70.
[25] X. Zhang, H. Su, X. Yang, Catalytic performance of a three-dimensionally ordered macroporous Co/ZrO2 catalyst in Fischer-Tropsch synthesis, J. Mol. Catal: A Chem. 360 (2012) 16–25.
[26] W. Zhang, Y. Cui, Z.G. Hu, W.L. Yu, J. Sun, N. Xu, Z.F. Ying, J.D. Wu, Structural, optical and electrical properties of high-k ZrO2 dielectrics on Si prepared by plasma assisted pulsed laser deposition, Thin. Solid. Films 520 (2012) 6361–6367.
[27] R. Zhang, X. Zhang, S. Hu, High temperature and pressure chemical sensors based on Zr/ZrO2 electrode prepared by nanostructured ZrO2 film at Zr wire, Sensor. Actuat: B Chem. 149 (2010) 143–154.
[28] A.B. Nawale, N.S. Kanhe, S.V. Bhoraskar, V.L. Mathe, A.K. Das, Influence of crystalline phase and defects in the ZrO2 nanoparticles synthesized by thermal plasma route on its photocatalytic properties, Mater. Res. Bull. 47 (2012) 3432–3439.
[29] A. Felix, V. Herdegen, R. Haseneder, J.U. Repke, Investigations on the behaviour of ceramic micro-and mesoporous membranes at hydrothermal conditions, Sep. Purif. Technol. 85–93 (2015).
[30] M.A. Waghmare, N.I. Beedri, A.U. Ubale, H.M. Pathan, Fabrication and characterization of rose bengal sensitized binary TiO2-ZrO2 oxides photo-electrode based dye-sensitized solar cell, Eng. Sci. (2019), https://doi.org/10.30919/es8d145 (in press).
[31] M. Waghmare, P. Sonone, P. Patil, H. Pathan, A. Ubale, Spray pyrolytic deposition of zirconium oxide thin films: influence of concentration on structural and optical properties, Eng. Sci. (2019), https://doi.org/10.30919/es8d622 (in press).
[32] I. Tsuji, H. Kato, H. Kobayashi Kudo, Photocatalytic H2 evolution reaction from aqueous solutions over band structure-controlled (AgIn)xZn2(1−x)S2 solid solution photocatalysts with visible-light response and their surface nanostructures, J. Am. Chem. Soc. 126 (2012) 13406–13413.
[33] A. Fathy, Investigation on microstructure and properties of Cu-ZrO2 nanocomposites synthesized by in situ processing, Mater. Lett. 213 (2018) 95–99.
[34] D. Bianchi, T. Chafik, M. Khalfallah, S.J. Teichner, Intermediate species on zirconia supported methanol aerogel catalysts: II. Adsorption of carbon monoxide on pure zirconia and on zirconia containing zinc oxide, Appl. Catal.: A Gen. 105 (1993) 223–249.
[35] G.H. Qin, Z. Sun, Q.P. Wu, L. Lin, M. Liang, S. Xue, Dye-sensitized TiO2 film with bifunctionalized zones for photocatalytic degradation of 4-cholophenol, J. Hazard. Mater. 192 (2011) 599–604.
[36] R.L.Z. Hoye, K.P. Musselman, MacManus-Driscoll, Research update: doping ZnO and TiO2 for solar cells, APL Mater. 1 (2013) 060701.
[37] L. Renuka, K.S. Anantharaju, Y.S. Vidya, H.P. Nagaswarupa, S.C. Prashantha, S.C. Sharma, A simple combustion method for the synthesis of multi-functional ZrO2/CuO nanocomposites: excellent performance as sunlight photocatalysts and enhanced latent fingerprint detection, Appl. Catal: B Environ. 217 (2017) 97–115.
[38] B.Q. Zhao, Q. Shao, L.H. Hao, L. Zhang, Z. Liu, B. Zhang, S.S. Ge, Yeast-template synthesized Fe-doped cerium oxide hollow microspheres for visible photodegradation of acid orange 7, J. Colloid. Interf. Sci 511 (2018) 39–47.
[39] W.X. Zhu, S.S. Ge, Q. Shao, Adsorption properties of ZrO2 hollow microboxes prepared using CaCO3 cubes as templates, RSC. Adv. 6 (2016) 81736–81743.
[40] Y.Y. Sheng, J. Yang, F. Wang, L.C. Liu, H. Liu, C. Yan, Z.H. Guo, Sol-gel synthesized hexagonal boron nitride/titania nanocomposites with enhanced photocatalytic activity, Appl. Surface Sci. 456 (2019) 154–163.
[41] J.K. Zhao, S.S. Ge, L.R. Liu, Q. Shao, X.M. Mai, Z.H. Guo, Microwave solvothermal fabrication of zirconia hollow microspheres with different morphologies using pollen templates and their dye adsorption removal, Ind. Eng. Chem. Res. 57 (2018) 231–241.
[42] M.Q. Fan, S.X. Hu, B. Ren, J. Wang, X.Y. Jing, synthesis of nanocomposite TiO2/ZrO2 prepared by different templates and photocatalytic properties for the photodegradation of Rhodamine B, Powder Technol. 235 (2013) 27–32.
[43] T.V.L. Thejaswini, D. Prabhakaran, M.A. Maheswari, Synthesis of mesoporous worm-like ZrO2-TiO2 monoliths and their photocatalytic applications towards organic dye degradation, J. Photoch. Photobio: A 344 (2017) 212–222.
[44] X.Y. Zhang, L. Li, S.S. Wen, H.X. Luo, C.L. Yang, Design and synthesis of multistructured three-dimensionally ordered macroporous composite bismuth oxide/zirconia: photocatalytic degradation and hydrogen production, J. Colloid. Interf. Sci 499 (2017) 159–169..
[45] H.L. Shindume, Z.Y. Zhao, N. Wang, H. Liu, A. Umar, J.X. Zhang, T.T. Wu, Z.H. Guo, Enhanced photocatalytic activity of B, N-codoped TiO2 by a new molten nitrate process, J. Nanosci. Nanotechnol. (2018), https://doi.org/10.1166/jnn.2018.15745 (in press).
[46] K.V.R. Chary, G.V. Sagar, D. Naresh, K.K. Seela, B. Sridhar, Characterization and reactivity of copper oxide catalysts supported on TiO2-ZrO2, J. Phys. Chem.: B 109 (2005) 9437–9444.
[47] M. Li, C.X. Li, G.L. Jiang, G.H. He, Hierarchically macro–mesoporous ZrO2/TiO2 composites with enhanced photocatalytic activity, Ceram. Int. 41 (2015) 5749–5757.
[48] J.K. Zhao, S.S. Ge, D. Pan, et al., Solvothermal synthesis, characterization and photocatalytic property of zirconium dioxide doped titanium dioxide spinous hollow microspheres with sunflower pollen as bio-templates, J. Colloid. Interf. Sci. 529 (2018) 111–121.

[49] W. Zheng, Z. Yan, Y. Dai, N.X. Du, X.B. Jiang, H.L. Dai, X.C. Li, G.H. He, Interpenetrated networks between graphitic carbon infilling and ultrafine TiO$_2$ nanocrystals with patterned macroporous structure for high-performance lithium ion batteries, ACS Appl. Mater. Int. 9 (2017) 20491–20500.

[50] X.J. Hou, X.F. Wang, B. Liu, Q.F. Wang, Z.R. Wang, SnO$_2$@TiO$_2$ heterojunction nanostructures for lithium-ion batteries and self-powered UV photodetectors with improved performances, Chemelectrochem 1 (2014) 300.

[51] T.H. Wu, Q. Shao, S.S. Ge, W.L. Zhao, Q.Y. Liu, Influence of molecular weight of chitosan on the microstructures and photocatalytic property of ZrO$_2$ prepared by chitosan templates method, Mater. Res. Bull. 83 (2016) 657–663.

[52] H. Choi, A.C. Sofranko, D.D. Dionysiou, Nanocrystalline TiO$_2$ photocatalytic membranes with a hierarchical mesoporous multilayer structure: synthesis, characterization, and multifunction, Adv. Funct. Mater. 16 (2006) 1067–1074.

[53] M.A. Behnajady, N. Modirshahla, M. Shokri, Photodestruction of Acid Orange 7 (AO7) in aqueous solutions by UV/H$_2$O$_2$: influence of operational parameters, Chemosphere 55 (2004) 129–134.

[54] H. Sudrajat, S. Babel, H. Sakai, S. Takizawa, Rapid enhanced photocatalytic degradation of dyes using novel N-doped ZrO$_2$, J. Environ. Manage. 165 (2016) 224–234.

[55] M.V. Carević, N.D. Abazović, T.B. Novaković, V.B. Pavlović, M.L. Čomor, Zirconium dioxide nanopowders with incorporated Si^{4+} ions as efficient photocatalyst for degradation of trichlorophenol using simulated solar light, Appl. Catal. B: Environ. 195 (2016) 112–120.

[56] W.W. Anku, S.O.B. Oppong, S.K. Shukla, E.S. Agorku, Palladium-doped–ZrO$_2$–multiwalled carbon nanotubes nanocomposite: an advanced photocatalyst for water treatment, Appl. Phys. A, Mater. 122 (2016) 579.

[57] F. Davar, A. Majedi, A. Abbasi, Synthesis of Fe$_3$O$_4$@ZrO$_2$ core–shell nanoparticles through new approach and its solar light photocatalyst application, J. Mater. Sci: Mater. El 28 (2017) 4871–4878.

[58] Y. Xu, M.A.A. Schoonen, The absolute energy positions of conduction and valence bands of selected semiconducting minerals, Am. Miner. (2000) 543–556.

[59] J.J. Zhang, Y.F. Gao, X.Y. Jia, J.Y. Wang, Z. Chen, X. Yu, Oxygen vacancy-rich mesoporous ZrO$_2$ with remarkably enhanced visible-light photocatalytic performance, Sol. Energ. Mat. Sol. C 182 (2018) 113–120.

[60] Z. Zhao, P. Bai, R. Guan, et al., Microstructural evolution and mechanical strengthening mechanism of Mg-3Sn-1Mn-1La alloy after heat treatments, Mater. Sci. Eng. A 734 (2018) 200–209.

[61] Y. Zhao, L. Qi, Y. Jin, K. Wang, J. Tian, P. Han, The structural, elastic, electronic properties and Debye temperature of D0$_{22}$-Ni$_3$V under pressure from first-principles, J. Alloys Compounds 647 (2015) 1104–1110.

[62] Y. Zhao, B. Zhang, H. Hou, W. Chen, M. Wang, Phase-field simulation for the evolution of solid/liquid interface front in directional solidification process, J. Mater. Sci. Technol. (2019), https://doi.org/10.1016/j.jmst.2018.12.009.

[63] Y. Zhao, S. Deng, H. Liu, J. Zhang, Z. Guo, H. Hou, First-principle investigation of pressure and temperature influence on structural, mechanical and thermodynamic properties of Ti$_3$AC$_2$ (A=Al and Si), Comput. Mater. Sci. 154 (2018) 365–370.

[64] Y. Zhao, X. Tian, B. Zhao, Y. Sun, H. Guo, M. Dong, H. Liu, X. Wang, Z. Guo, A. Umar, H. Hou, Precipitation sequence of middle Al concentration alloy using the inversion algorithm and microscopic phase field model, Sci. Adv. Mater. 10 (2018) 1793–1804.

[65] C. Wang, Z. He, X. Xie, et al., Controllable cross-linking anion exchange membranes with excellent mechanical and thermal properties, Macromol. Mater. Eng. 3 (2018) 1700462.

[66] C. Wang, B. Mo, Z. He, et al., Crosslinked norbornene copolymer anion exchange membrane for fuel cells, J. Membrane Sci. 556 (2018) 118–125.

[67] C. Wang, B. Mo, Z. He, et al., Hydroxide ions transportation in polynorbornene anion exchange membrane, Polymer 138 (2018) 363–368.

[68] Z. Qu, M. Shi, H. Wu, Y. Liu, J. Jiang, C. Yan, An efficient binder-free electrode with multiple carbonized channels wrapped by NiCo$_2$O$_4$ nanosheets for high-performance capacitive energy storage, J. Power Sources 410–411 (2019) 179–187.

[69] Z. Wang, H. Zhu, N. Cao, R. Du, Y. Liu, G. Zhao, Superhydrophobic surfaces with excellent abrasion resistance based on benzoxazine/mesoporous SiO$_2$, Mater. Lett. 186 (2017) 274–278.

[70] C. Wang, V. Murugadoss, J. Kong, et al., Overview of carbon nanostructures and nanocomposites for electromagnetic wave shielding, Carbon 140 (2018) 696–733.

[71] D. Jiang, V. Murugadoss, Y. Wang, et al., Electromagnetic interference shielding polymers and nanocomposites – a review, Polym. Rev. (2018), https://doi.org/10.1080/15583724.2018.1546737 (in press).

[72] W. Du, X. Wang, J. Zhan, X. Sun, L. Kang, F. Jiang, X. Zhang, Q. Shao, M. Dong, H. Liu, V. Murugadoss, Z. Guo, Biological cell template synthesis of nitrogen-doped porous hollow carbon spheres/MnO$_2$ composites for high-performance asymmetric supercapacitors, Electrochim. Acta 296 (2019) 907–915.

[73] M. Idrees, S. Batool, J. Kong, et al., Polyborosilazane derived ceramics – nitrogen sulfur dual doped graphene nanocomposite anode for enhanced lithium ion batteries, Electrochim. Acta 296 (2019) 925–937.

[74] M. Dong, Q. Li, H. Liu, et al., Thermoplastic polyurethane-carbon black nanocomposite coating: fabrication and solid particle erosion resistance, Polymer 158 (2018) 381–390.

[75] B. Kirubasankar, V. Murugadoss, J. Lin, et al., In-situ grown nickel selenide onto graphene nanohybrid electrodes for high energy density asymmetric supercapacitors, Nanoscale 10 (2018) 20414–20425.

[76] W. Zhao, X. Li, R. Yin, L. Qian, X. Huang, H. Liu, J. Zhang, J. Wang, T. Ding, Z. Guo, Urchin-like NiO-NiCo$_2$O$_4$ heterostructure microsphere catalysts for enhanced rechargeable non-aqueous Li-O$_2$ batteries, Nanoscale 11 (2019) 50–59.

[77] H. Du, C. Zhao, J. Lin, et al., Carbon nanomaterials in direct liquid fuel cells, Chem. Rec. 18 (2018) 1365–1372.

[78] Z. Zhao, H. An, J. Lin, et al., Progress on the photocatalytic reduction removal of chromium contamination, Chem. Rec. (2019), https://doi.org/10.1002/tcr.201800153. in press.

[79] H. Gu, H. Zhang, J. Lin, et al., Large negative giant magnetoresistance at room temperature and electrical transport in cobalt ferrite-polyaniline nanocomposites, Polymer 143 (2018) 324–330.

[80] Z. Li, B. Wang, X. Qin, et al., Superhydrophobic/superoleophilic polycarbonate/carbon nanotubes porous monolith for selective oil adsorption from water, ACS Sustain. Chem. Eng. 6 (2018) 13747–13755.

[81] L. Wang, H. Qiu, C. Liang, P. Song, Y. Han, Y. Han, J. Gu, J. Kong, D. Pan, Z. Guo, Electromagnetic interference shielding MWCNT-Fe$_3$O$_4$@Ag/epoxy nanocomposites with satisfactory thermal conductivity and high thermal stability, Carbon 141 (2019) 506–514.

[82] H. Gu, H. Zhang, C. Ma, et al., Trace electrosprayed nanopolystyrene facilitated dispersion of multiwalled carbon nanotubes: simultaneously strengthening and toughening epoxy, Carbon 142 (2019) 131–140.

[83] N. Wu, C. Liu, D. Xu, et al., Ultrathin high-performance electromagnetic wave absorbers with facilely fabricated hierarchical porous Co/C crabapples, J. Mater. Chem. C (2019), https://doi.org/10.1039/C8TC04984J. in press.

[84] Y. Qian, Y. Yuan, H. Wang, et al., Highly efficient uranium adsorption by salicylaldoxime/polydopamine graphene oxide nanocomposites, J. Mater. Chem. A 6 (2018) 24676–24685.

[85] H. Liu, Q. Li, S. Zhang, et al., Electrically conductive polymer composites for smart flexible strain sensor: a critical review, J. Mater. Chem. C 6 (2018) 12121–12141.

[86] H. Wei, H. Wang, Y. Xia, et al., An overview of lead-free piezoelectric materials and devices, J. Mater. Chem. C 6 (2018) 12446–12467.

[87] Z. Wu, Z. Hui, L. Chen, et al., Interfacially reinforced unsaturated polyester carbon fiber composites with a vinyl ester-carbon nanotubes sizing agent, Compos. Sci. Technol. 164 (2018) 195–203.

[88] P. Xie, B. He, F. Dang, et al., Bio-gel derived nickel/carbon nanocomposites with enhanced microwave absorption, J. Mater. Chem. C 6 (2018) 8812–8822.

[89] N. Wu, C. Liu, D. Xu, et al., Enhanced electromagnetic wave absorption of three-dimensional porous Fe$_3$O$_4$/C composite flowers, ACS Sustain. Chem. Eng. 6 (2018) 12471–12480.